Thin-Walled Structures 129 (2018) 457–472

Contents lists available at ScienceDirect

Thin-Walled Structures

journal homepage: www.elsevier.com/locate/tws

Full length article

Crashworthiness optimization with uncertainty from surrogate model and numerical error

Na Qiu[a,b], Yunkai Gao[c,*], Jianguang Fang[d,e], Guangyong Sun[e], Qing Li[e], Nam H. Kim[b,*]

[a] Mechanical and Electrical Engineering College, Hainan University, Haikou 570228, China
[b] Dept. of Mechanical & Aerospace Engineering, University of Florida, Gainesville, FL 32611, USA
[c] School of Automotive Studies, Tongji University, Shanghai 201804, China
[d] Centre for Built Infrastructure Research, School of Civil and Environmental Engineering, University of Technology Sydney, Sydney, NSW 2007, Australia
[e] School of Aerospace, Mechanical and Mechatronic Engineering, The University of Sydney, Sydney, NSW 2006, Australia

ARTICLE INFO

Keywords:
Crashworthiness
Surrogate model
Optimization
Numerical uncertainty

ABSTRACT

Due to the expensive cost of full-scale tests, more and more designs rely on simulation. For highly nonlinear crash simulation, numerical uncertainty is an inherent by-product, which refers to the oscillation of results when the simulation is repeated at the same design or the design variables are slightly changed. This oscillation directly influences the quality and reliability of the optimal design. This paper shows how these issues can be addressed by proposing a simple uncertainty quantification method for numerical uncertainty (noise) and surrogate model uncertainty (error) in the optimization process. Three engineering problems, a tube crush example, an automotive front-rail crush example and a multi-cell structure crush example, are used to illustrate this method. Firstly, the level of numerical uncertainty is quantified in terms of noise frequency and amplitude, and the convergence study of these two criteria is employed to determine an appropriate data size to describe numerical noise. Secondly, an estimation method considering both numerical noise and surrogate model error is proposed based on the prediction variance of the polynomial response surface. Finally, the tube and front rail structures are optimized according to the proposed uncertainty quantification method. It was found that by considering the two sources of uncertainty, the optimal designs are more reliable than the deterministic solutions.

1. Introduction

Vehicle crashworthiness has drawn increasing attention because it is associated with public safety and socioeconomic benefits. One possible way to enhance crashworthiness is to optimize the energy absorption capability of key automotive components, thereby reducing severe injuries and fatalities when a collision occurs. With the increase of speed and power of computers in recent years, the ability to simulate complex systems has been improved [1], which facilitates crashworthiness optimization in aerospace and automotive engineering fields. Despite the wide use of finite element analysis in crashworthiness optimization, the presence of numerical uncertainty (noise) requires more attention.

Here, numerical uncertainty (noise) represents the oscillations with small wavelengths when the same simulation model is calculated several times or the design variables are slightly changed. Many researchers [2–4] pointed out that the crash simulations are not repeatable and have obvious numerical uncertainty due to the instability of structures (such as buckling) [2], contact bifurcations, numerical rounding errors and parallel computing errors [5]. Thole and Mei [6] revealed that the unstable behavior or large numerical noise in crash simulations is due to bifurcations, which in turn are caused by parallel computing algorithms, contact search problems, buckling, and levers. Will and Bucher [7] revealed the existence of numerical noise in front-crash load case for a passenger vehicle and proposed a method to identify and quantify the numerical noise. Duddeck [3] claimed that the level of noise in the crash simulation varies from 1% to 10%, which depends on the FE model, configuration, and load cases. They also assumed that frontal impact load case is much more sensitive to bifurcations than the lateral load case. Therefore, in this paper, we will use the tube and front rail models as examples to quantify the numerical noise and to take into account it in the crashworthiness optimization process.

Many existing studies are limited to deterministic optimization. However, there are a number of uncertainties which must be compensated during the optimization process. For uncertainty-based optimization, most researchers [8–16] mainly considered the parametric

* Corresponding authors.
E-mail addresses: gaoyunkai@tongji.edu.cn (Y. Gao), nkim@ufl.edu (N.H. Kim).

https://doi.org/10.1016/j.tws.2018.05.002
Received 31 July 2017; Received in revised form 9 February 2018; Accepted 1 May 2018
0263-8231/

uncertainty in sheet thickness, geometry size and mechanical properties of materials due to manufacturing imperfection and/or other factors. However, surrogate model uncertainty may have a large effect on the reliability and robustness of the optimum and should be taken into account in the optimization process [17,18]. In this regard, Picheny et al. [19] developed a conservative surrogate method by adding a safety margin to consider the surrogate model uncertainty. Viana et al. [20] investigated the conservative modeling technique to consider the model form error by using cross validation method. Zhang et al. [17] proposed a new robust design method based on the prediction variance of kriging model to take into account both surrogate model uncertainty and parametric uncertainty. Kim and Choi [21] discussed a reliability-based design optimization method including the effect of response surface error. However, the previous studies on crashworthiness optimization often focus on input randomness and surrogate model error and fail to consider the effect of numerical uncertainty. For constrained optimization problems, the optimum solution tends to be pushed on the constraint boundary, which leaves a little room to tolerate the prediction error of surrogate model and numerical uncertainty. Therefore, the numerical uncertainty and surrogate model uncertainty need to be considered to ensure reliable optimal design.

Even if we know the presence of numerical uncertainty in crashworthiness simulation, it is unclear how to quantify its level, how to determine the suitable data size to quantify it, and how to obtain reliable optimums. All of these are the difficulties that need to be solved when considering numerical uncertainty in engineering applications. This paper aims to address these issues by following the flowchart as shown in Fig. 1. The paper is structured as follows: Section 2 reveals the presence of numerical uncertainty in crashworthiness simulations and quantifies the level of numerical noise according to the frequency and amplitude of noise. Based on these two criteria, the sample size is determined from the convergence study. The estimation method for both numerical and surrogate model uncertainties is discussed in detail in Section 3. Section 4 aims to develop an uncertainty-based optimization methodology by considering both numerical uncertainty and surrogate model uncertainty, followed by conclusions in Section 5.

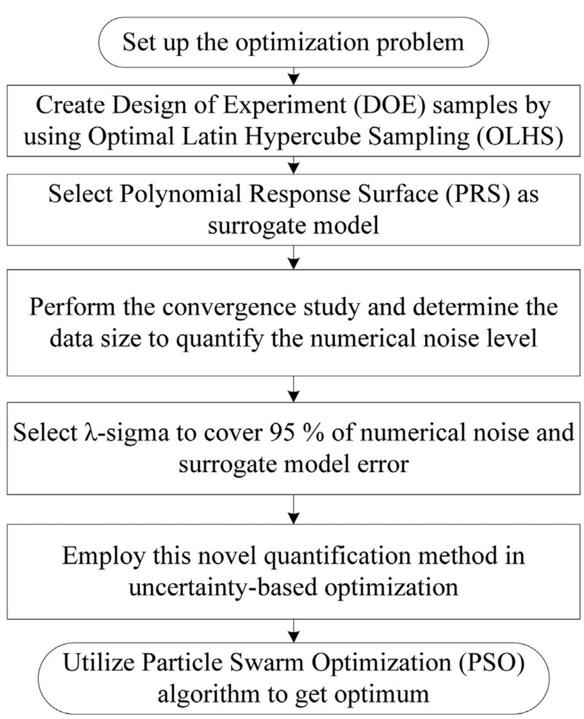

Fig. 1. The flowchart of dealing with numerical noise in uncertainty-based crashworthiness optimization.

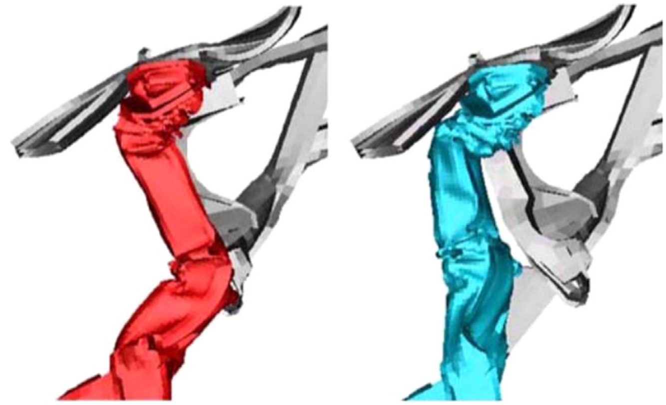

Fig. 2. Example of a frontal crash simulation with the same FE model and hardware shows two different reaction patterns because of bifurcation [22].

2. Determination of data size to quantify numerical noise

Because of the expensive cost of full-scale tests, most of crashworthiness optimizations are conducted based on computer simulations. However, most commercial programs for simulating crashworthiness use an explicit time integration scheme, a penalty-based contact/impact formulation, and distributed memory parallelization. For the highly nonlinear nature of crashworthiness simulation, the objective functions are often non-convex, with a number of extrema and discontinuities [5]. For these reasons, the simulation results are subjected to significant numerical error and noise, which is considered as the main difficulty in crashworthiness optimization and largely affects the reliability and robustness of optimum designs. Numerical uncertainty means that different runs at different times or machines yield different results. Even with the same FE model and hardware, the simulation results can be different [3,22], as shown in Fig. 2. Therefore, the response of a design cannot be represented by the value from one simulation, but a confidence interval considering numerical uncertainty, which can yield more robust and reliable optimums for crashworthiness optimization.

2.1. Problem description

In this study, specific energy absorption (*SEA*) is considered as an objective function to quantitatively evaluate the crash performances. *SEA* is a key indicator to take into account the energy absorption capability and the mass factor, and can be calculated from the following formula:

$$SEA = \frac{EA}{M} = \frac{\int_0^d F(s)\mathrm{d}s}{M} \tag{1}$$

where F is the impact force at the crash distance s and d is the total crash displacement concerned. EA is the energy absorption at the displacement d. The crash performance of the front rail performs better when it can absorb more energy so that less energy is transferred to passengers in the event of a crash. At the same time, light weight is preferable for the lightweight requirement. In this study, d is set to 120 mm for tube and multi-cell structure and 150 mm for front rail examples, respectively.

2.1.1. Tube crash example

In this paper, a square tube under axial compressive loading (see Fig. 3) is used as an example to study how to deal with the numerical error and noise in crashworthiness. Since the energy absorber in the front rail is a tube-like structure, some researchers [13,23–29] have previously investigated the tube structure in order to improve the crashworthiness performance of the front rail. As an important energy

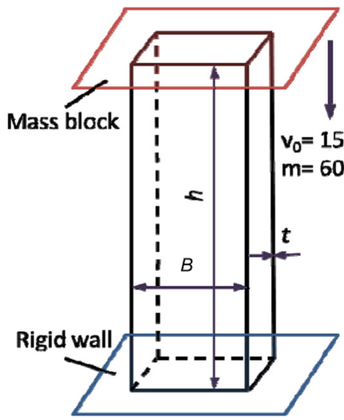

Fig. 3. An aluminum square tube under axial loading.

absorber, front rails of automobiles and trains need to be optimized to protect passengers from fatal or severe injuries during the collision.

The height h of this tube is 150 mm, and the width B and the thickness t are considered as design variables, whose values are determined according to the size of a front rail for the vehicle. The tube impacts onto a rigid wall at the bottom end with an initial velocity of $v_0 = 15$ m/s. To consider the effect of entire vehicle, an additional mass of 600 kg is attached to the tube's top end. The loading and boundary condition is set in order to simulate the crash performance of the front rail (tube structure) under typical crash conditions. The tube geometry was modeled with the Belytschko-Tsay reduced integration shell elements [30] with five integration points through the thickness, which can represent the thickness change by a relaxation of the thickness variable. The mesh size was determined to be close to 2 mm based on a mesh convergence study. To avoid volumetric locking and spurious zero energy deformation modes, reduced integration and stiffness-based hourglass control were employed in the simulation model. Two types of contact were used to avoid penetrations in the FE model. "Automatic single surface" contact was utilized to model the self-contact of the tube during the folding and "Automatic node to surface" was used to simulate the interactions between the tube and the rigid supports. The Coulomb friction coefficients for all contact surfaces were set to be 0.15 [31].

As a lightweight material commonly used for energy absorbers, aluminum is used with the following mechanical properties: density $= 2700\ \mathrm{kg/m^3}$, Poisson's ratio $= 0.29$, Young's modulus $= 68.2$ GPa, initial yield stress $= 227$ MPa and tangent modulus $= 312$ MPa. An elastoplastic material model 123 in LS-DYNA with linear hardening was used to describe the constitutive behavior of the thin-walled structure.

Therefore, the optimization problem can be formulated as follows:

$$\begin{cases} \min\ -SEA(B, t) \\ s.\ t. \quad F_{\max}(B, t) \le 65\mathrm{kN} \\ \quad 40\ \mathrm{mm} \le B \le 80\ \mathrm{mm} \\ \quad 1.5\ \mathrm{mm} \le t \le 2.5\ \mathrm{mm} \end{cases} \tag{2}$$

where F_{max} is the maximum force applied during the process. The negative sign in the design criterion *SEA* is used so that it is maximized during optimization.

2.1.2. Frontal side rail example

To explore the performance of the proposed uncertainty estimation method in the industry context, a frontal side rail structure of 2010 Toyota Yaris sedan was utilized as shown in Fig. 4. This passenger vehicle was originally created for frontal crash simulations and was validated by NCAC (National Crash Analysis Center) [32]. The front rail structure (see Fig. 4) was extracted from the full vehicle for the study purpose.

The design variables t_1 and t_2 are the thicknesses of two parts of absorber box. The number of nodes and elements of the front rail baseline model were 90708 and 6642, respectively. To keep the same element formulation with the original NCAC model, fully integrated shell element with 3 integration points through thickness was employed. The contact modeling technique and friction coefficients were similar to that of the tube model. The material properties are also unchanged from the NCAC model. The front rail structure was modeled through a piecewise linear elastic-plastic behavior with strain hardening (Material model 24 in LS-DYNA). The material for the absorber box is steel, with the following mechanical properties: density $= 7800\ \mathrm{kg/m^3}$, Poisson's ratio $= 0.3$, Young's modulus $= 200$ GPa, yield stress $= 380$ GPa, and the relationship between true stress and plastic strain was defined in Fig. 5. Cowper-Symonds was utilized to consider the strain rate effect.

The optimization problem is to maximize the *SEA* while constraining the peak force lower than a threshold level:

$$\begin{cases} \min\ -SEA(t_1, t_2) \\ s.\ t. \quad F_{\max}(t_1, t_2) \le 160\mathrm{kN} \\ \quad 0.7\ \mathrm{mm} \le t_1 \le 2.5\ \mathrm{mm} \\ \quad 0.7\ \mathrm{mm} \le t_2 \le 2.5\ \mathrm{mm} \end{cases} \tag{3}$$

The threshold force of 160 kN was obtained from the base model with original thicknesses of 1.89 mm and 1.30 mm for t_1 and t_2, respectively. The bottom side of the rail was constrained to a rigid wall. The impactor with a mass of 600 kg was impacted onto the front end of absorber box with an impact velocity of 15 m/s. The material of the absorber box and frontal side rail are all steel.

2.1.3. Multi-cell tube example

In reality, engineering optimization problems involve many design variables. To demonstrate the performance of the proposed method for many design variables, a multi-cell hexagonal tube structure with seven design variables was used as the third example in this paper as shown in Fig. 6. The cross-sectional configuration is proposed based on the optimal design from reference [33]. For the multi-cell tube crush example, the mesh size was set as 1.5 mm and six elements were used along each edge of the small triangular cells in the multi-cell cross-section shown in Fig. 6. The Belytschko-Tsay reduced integration shell elements with ten integration points through the thickness was employed to model the multi-cell tube.

The FE model for multi-cell tube crash example was similar to the tube example but with the different cross-sectional configuration. There are seven design variables T_1–T_7, which represent different thicknesses for different ribs or walls (see Fig. 6). The optimization problem is to maximize the energy absorption (*EA*) and constrain the $F_{\max}$ lower than a threshold level:

$$\begin{cases} \min\ -EA(T_1, T_2, T_3, T_4, T_5, T_6, T_7) \\ s.\ t. \quad F_{\max}(T_1, T_2, T_3, T_4, T_5, T_6, T_7) \le 160\mathrm{kN} \\ \quad 1.0\ \mathrm{mm} \le T_1, T_2, T_3, T_4, T_5, T_6, T_7 \le 2.0\ \mathrm{mm} \end{cases} \tag{4}$$

As this multi-cell structure aims to be applied to the absorber structure in the front-rail, the constraint of $F_{\max}$ is selected the same one with the front-rail example, 160 kN.

2.2. Polynomial response surface for noisy data

This section explains the proposed method of building a surrogate and compensating numerical and model uncertainties using the tube crush example. Since crashworthiness optimization is computationally expensive, surrogate models are often employed to reduce the number of simulations. Some surrogate models also help the optimization process because they tend to filter out the random numerical noise, especially for gradient-based optimization algorithms. However, other surrogate models, such as interpolative surrogate models, are easily affected by numerical noise. In addition, even if the structural response

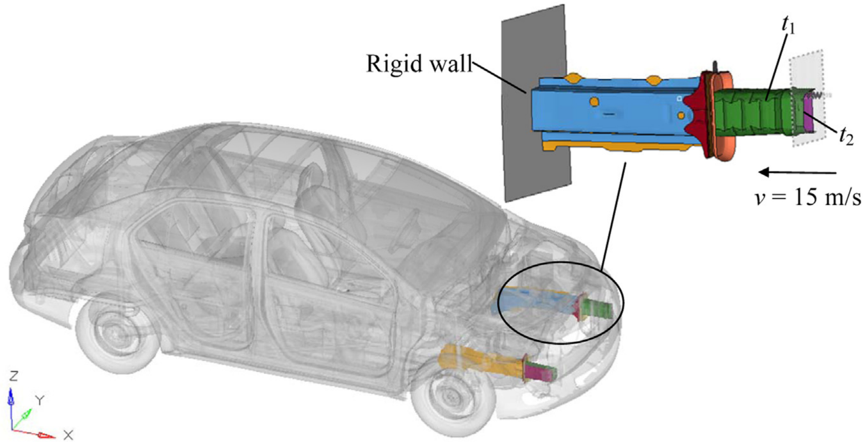

Fig. 4. Model of automotive front-rail structure of 2010 Toyota Yaris sedan.

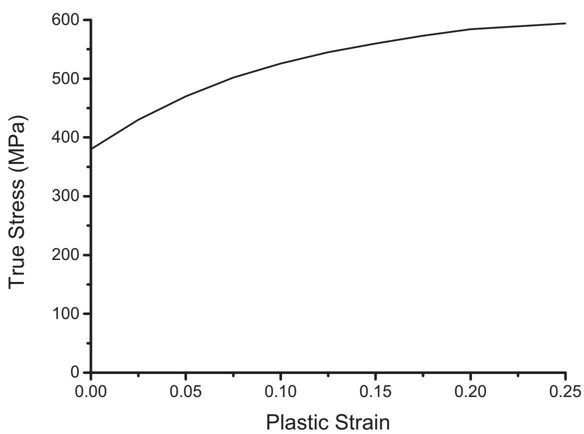

Fig. 5. Relationship between plastic strain and true stress for front rail model.

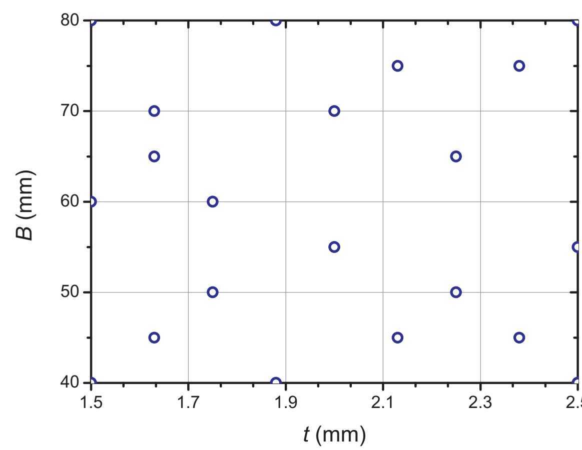

Fig. 7. Training points for the tube example.

is highly nonlinear, design criteria are mildly nonlinear with respect to design variables. Therefore, in this paper, a polynomial response surface (PRS), one of the commonly used regression surrogate models, is selected as the surrogate model to filter out numerical noise [34].

The optimal Latin hypercube sampling (OLHS) technique [35] was employed to generate 20 sample points in addition to 4 corner points in the two-dimensional design space (see Fig. 7). PRS was used to approximate the responses of *SEA* and $F_{\max}$ by utilizing the above-mentioned 24 sampling points. In order to assess the accuracy of the surrogate models in the whole design space, 21 × 21 = 441 points with uniform intervals were used as test points. Note that in practice, 441 samples are not required to build the surrogate; they are used for the purpose of validation. The coefficient of determination (R^2) and the adjusted coefficient of determination ($\overline{R}^2$) were used to evaluate the

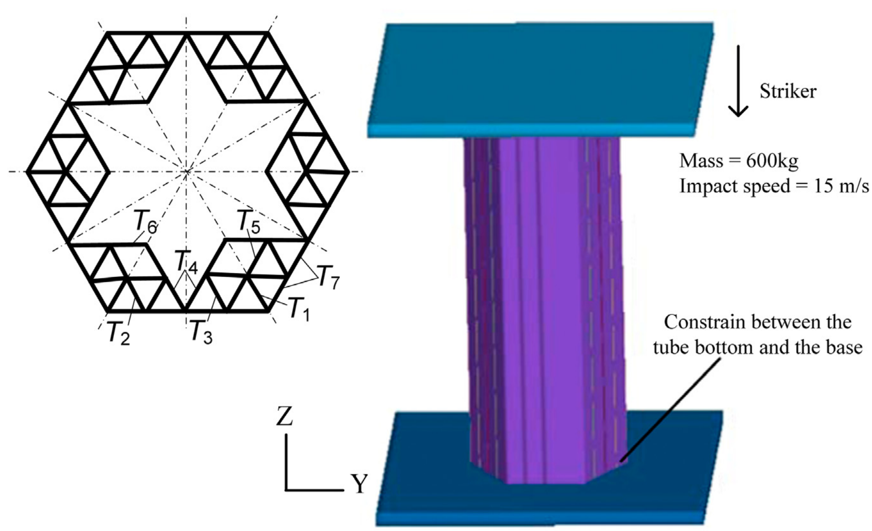

Fig. 6. FE model and design variables for the multi-cell tube crash example.

Table 1
Accuracy comparison of different orders of PRS surrogate models.

		First-order PSR	Second-order PRS	Third-order PRS
$F_{\max}$	R^2	0.980	0.984	0.983
	Adjusted $\overline{R}^2$	0.978	**0.979**	0.972
SEA	R^2	0.940	0.950	0.955
	Adjusted $\overline{R}^2$	0.934	**0.936**	0.927

accuracy of the surrogate models. To be specific, the R^2 and $\overline{R}^2$ in Table 1 are calculated from the 441 test points according to Eqs. (5) and (6), respectively.

$$R^2 = 1 - \frac{\sum_{i=1}^{N_v} (y_i - \widehat{y_i})^2}{\sum_{i=1}^{N_v} (y_i - \overline{y})^2} \tag{5}$$

$$\overline{R}^2 = 1 - \frac{(1 - R^2)(n - 1)}{(n - p - 1)} \tag{6}$$

where y_i and $\widehat{y_i}$ are the exact function value and the corresponding surrogate value for assessment point i, respectively. $\overline{y}$ is the mean of y_i, N_v denotes the number of the test sampling points. n is the total sample size and p is the number of coefficients in the PRS model.

In general, the values of R^2 and $\overline{R}^2$ close to 1 are preferred, indicating a high accuracy for overall performance in the design space. The orders of polynomial models were selected mainly based on the adjusted $\overline{R}^2$ to compensate the increases of the number of coefficients. The orders of polynomial models were selected mainly based on the adjusted $\overline{R}^2$ to compensate the increases of the number of coefficients. As shown in Table 1, the second-order PRS performs best in terms of accuracy, which is therefore used in the following analysis process. It can be seen that the second-order PRS was validated in approximating the *SEA* and $F_{\max.}$ In this case, the $\overline{R}^2$ was evaluated as 97.9% and 93.6% for $F_{\max}$ and *SEA*, respectively.

To gain more insights into PRS models, the 3D contours of $F_{\max}$ and *SEA* are plotted in Fig. 8. We also plot the actual simulation results of *SEA* and $F_{\max}$ over the design space by using the 441 test points of equal intervals. As shown in Fig. 8(c) and (d), the simulation results reveal a significant level of numerical noise. It means a small change in the design variables can result in a large change in simulation results. This numerical noise is present due to the bifurcations, the lack of convergence in explicit time integration, parallel computing algorithm, contact search problems, buckling, and levers. In the presence of a large error, PRS proves to be suitable for its characteristic of filtering out the noise as shown in Fig. 8(a) and (b). However, it is noted that other surrogates, such as Kriging with nugget, can also consider noise in data.

Another important observation is that between the two design variables, t and B, numerical solutions oscillated significantly in the width direction (B) than in the thickness direction (t), as shown in Fig. 8(d). This is because the finite element mesh remains the same when the thickness of the plate changes, while the size and the number of mesh change when the width changes. This error/noise has to be considered in order to maintain the reliability and robustness of the optimal design.

2.3. Data size for quantifying numerical noise

As shown in Fig. 8(c) and (d), the random oscillations of numerical noise were observed with the increase of t and B. However, it is hard to interpret this characteristic from visual inspection and there is a need to quantify the noise level. The numerical uncertainty (noise) level can be decomposed into two factors: the frequency and amplitude [1]. The former is defined by the percentage oscillations frequency, f_r, formulated as

$$f_r = 100 \frac{\sum_{i=1}^{n} \Omega_i}{n} \tag{7}$$

where Ω_i is used to evaluate the oscillation parameters for the ith sample when the total number of samples is equal to n. For the ith sample, if the sign of the gradient changes at that point, then $\Omega_i = 1$. Therefore, $f_r = 0$ donates a very stable signal where all the samples monotonically change and $f_r = 100$ represent a fully oscillatory signal where the gradient changes its sign for every point.

Another important characteristic of noise is the amplitude. The amplitude accounts for the magnitude of each individual oscillation. Two-sigma rule design in statistics was adopted in this study. Considering the randomness in the data, two-sigma is an adequate measure of data spread because it can account for 95% of the recorded data, which is used to define the amplitude of noise $A_{2\sigma}$, given as

$$A_{2\sigma} = 2\sigma \tag{8}$$

where σ is the standard deviation of selected samples. For the tube example, 101 sample points were finally selected to evaluate the level of numerical noise based on the convergence study of different sample sizes. The FEA results are regarded as the random result for that point and their prediction result from PRS is regarded as the mean value because it filters out the numerical noise. The standard deviation can be estimated from the standard error of the PRS.

But in practical engineering application, one difficulty in quantifying the numerical noise is to determine the sample size. It is obvious that the more samples the better, but it is related to the computational cost. This paper proposes a method of convergence study to determine the appropriate sample size based on the above-mentioned two criteria. By taking the tube example, we compared the frequency and amplitude for sample sizes of 25, 34, 51 and 101 by equally distributing samples for the design range of t and B. The convergence can be evaluated based on the difference in frequency or amplitude divided by the sample size difference. As shown in Fig. 9(a-d), when sample size increased to 101 (the change intervals are 0.01 mm for thickness t and 0.4 mm for width B), the relative difference of frequency and amplitude on different data size are all less than 15%. Thus, the sample size 101 was selected as the convergence value of the sample size for both *SEA* and $F_{\max}$. Overall, the total number of FE simulations is 226 (24 for building the PRS surrogate models and 101 × 2 for quantifying numerical noise of B and t) for the tube crash example.

On the other hand, the selection of sample size should also consider the tradeoff between the accuracy and computational efficiency. As shown in Fig. 9(e-h), some frequency and amplitude of front-rail example have not converged even when the sample size increased to 73. The front rail example needs comparatively high computational cost. For this reason, the sample size of 73 is adopted for the evaluation of numerical noise in this case. Therefore, the total number of FE simulations for the front rail example is 170 (24 for building the PRS surrogate models and 73 × 2 for quantifying the numerical noise of t_1 and t_2). Based on the convergence study, it is clear that the initial 24 samples are not sufficient to estimate the level of numerical noise. Therefore, it is expected that there is a discrepancy between the actual numerical noise level and the level of noise that the surrogate model estimates. It also can be observed in Fig. 9 that the amplitude of numerical noise for t (see Fig. 9(d)) is smaller than that of B (see Fig. 9(b)) due to the change of element size when the width B changes, which has been discussed in Section 2.2.

For the multi-cell structure example, the frequency and amplitude were compared for sample sizes of 13, 16, 20, 33 and 51 by equally distributing samples for design range of each T_1–T_7, when other design variables are fixed at 1.0 mm. As shown in Fig. 10, the noise amplitude of 7 design variables for $F_{\max}$ and *EA* all converged well when the data size increased to 51. However, the noise frequency for $F_{\max}$ and *EA* of some design variables (for example T_1 and T_2 in Fig. 10c) are still not converged well. As mentioned above, the tradeoff between the accuracy

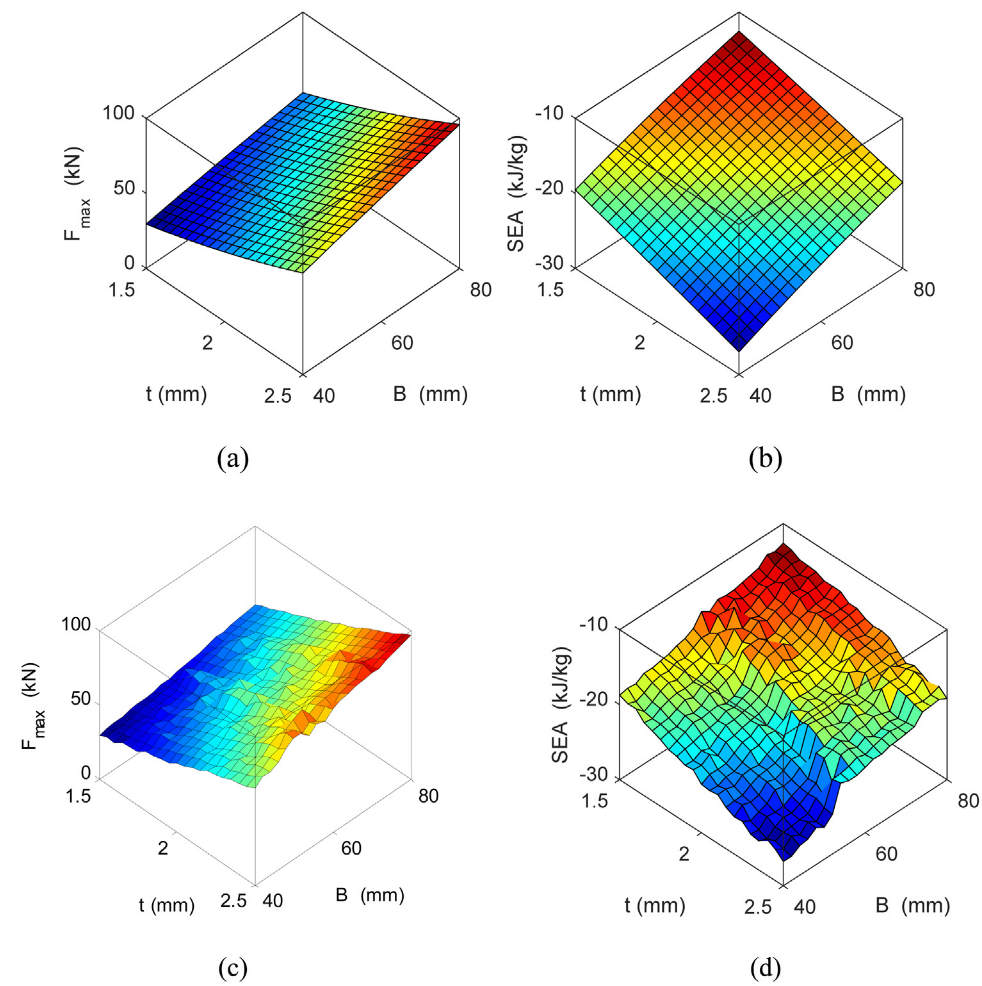

Fig. 8. 3D surfaces of $F_{\max}$ and *SEA*: (a) $F_{\max}$ for PRS; (b) *SEA* for PRS; (c) $F_{\max}$ plot directly from the 441 sample data; (d) *SEA* plot directly from the 441 sample data.

and computational efficiency need to be considered. More importantly, the amplitude is highly related to the noise level and is more important than the frequency for the quantifying process. Therefore, data size 51 was utilized as the data size to quantify the numerical noise for the multi-cell structure example.

3. Estimation of numerical noise based on PRS surrogate model

3.1. Estimation of numerical noise and surrogate model error for the tube structure

Based on the convergence study, we can consider the effect of numerical noise in the optimization process. At the same time, the surrogate model uncertainty can also be taken into account. Surrogate model uncertainty refers to the discrepancy between the metamodel prediction and simulated responses, which normally is an inevitable source of uncertainty in surrogate-based optimization. PRS is a common linear regression model, which is described in a linear combination of the vector of known basis functions $\boldsymbol{\xi}(\mathbf{x})$ and the vector of unknown coefficients $\mathbf{b}$ as [36]

$$\hat{y}(\mathbf{x}, \mathbf{b}) = \boldsymbol{\xi}(\mathbf{x})\cdot\mathbf{b} \tag{9}$$

The standard error, which represents the standard deviation of random error between data and PRS predictions, can be expressed as

$$\hat{\sigma} = \sqrt{\frac{\mathbf{e}^{\mathrm{T}}\mathbf{e}}{n_y - n_b}} \tag{10}$$

where $\mathbf{e}$ is the vector of errors between the surrogate predictions and the data, n_y is the number of data and n_b is the number of coefficients. Using the standard error, the prediction variance at a point $\mathbf{x}$ can be calculated as

$$\sigma^2 = \hat{\sigma}^2[\boldsymbol{\xi}(\mathbf{x})^{\mathrm{T}}(\mathbf{X}^{\mathrm{T}}\mathbf{X})^{-1}\boldsymbol{\xi}(\mathbf{x})] \tag{11}$$

where $\mathbf{X}$ is the design matrix composed of the basis vector at sampling points. It was observed that the prediction variance is not only related to the standard error of the sampling points but also the position of the prediction point. In general, the surrogate model uncertainty of PRS is assumed to be normally distributed with the mean at prediction value in Eq. (8) and the variance in Eq. (10).

In this study, it is assumed that uncertainty in the surrogate prediction comes from two sources. One is surrogate model uncertainty due to sampling error and model form error, which is the error between surrogate predictions and simulation results. The other is numerical uncertainty due to randomness in simulation results. Let $y_{\mathrm{true}}(\mathbf{x})$ be the true response, $y_{\mathrm{sim}}(\mathbf{x})$ the simulation output, and $y_{\mathrm{surr}}(\mathbf{x})$ the surrogate prediction. The relationship between them can be written as

$$y_{\mathrm{sim}}(\mathbf{x}) = y_{\mathrm{surr}}(\mathbf{x}) + e_{\mathrm{surr}} \tag{12}$$

$$y_{\mathrm{true}}(\mathbf{x}) = y_{\mathrm{sim}}(\mathbf{x}) + e_{\mathrm{num}} \tag{13}$$

where e_{surr} and e_{num} are, respectively, the surrogate error and numerical noise. In general, the simulation also has a model error or systematic bias, but it is ignored in this paper as the purpose is not comparing the results with physical tests. These errors include both aleatory uncertainty (variability or random) and epistemic uncertainty (model form error or bias). By combining the two equations, we can estimate

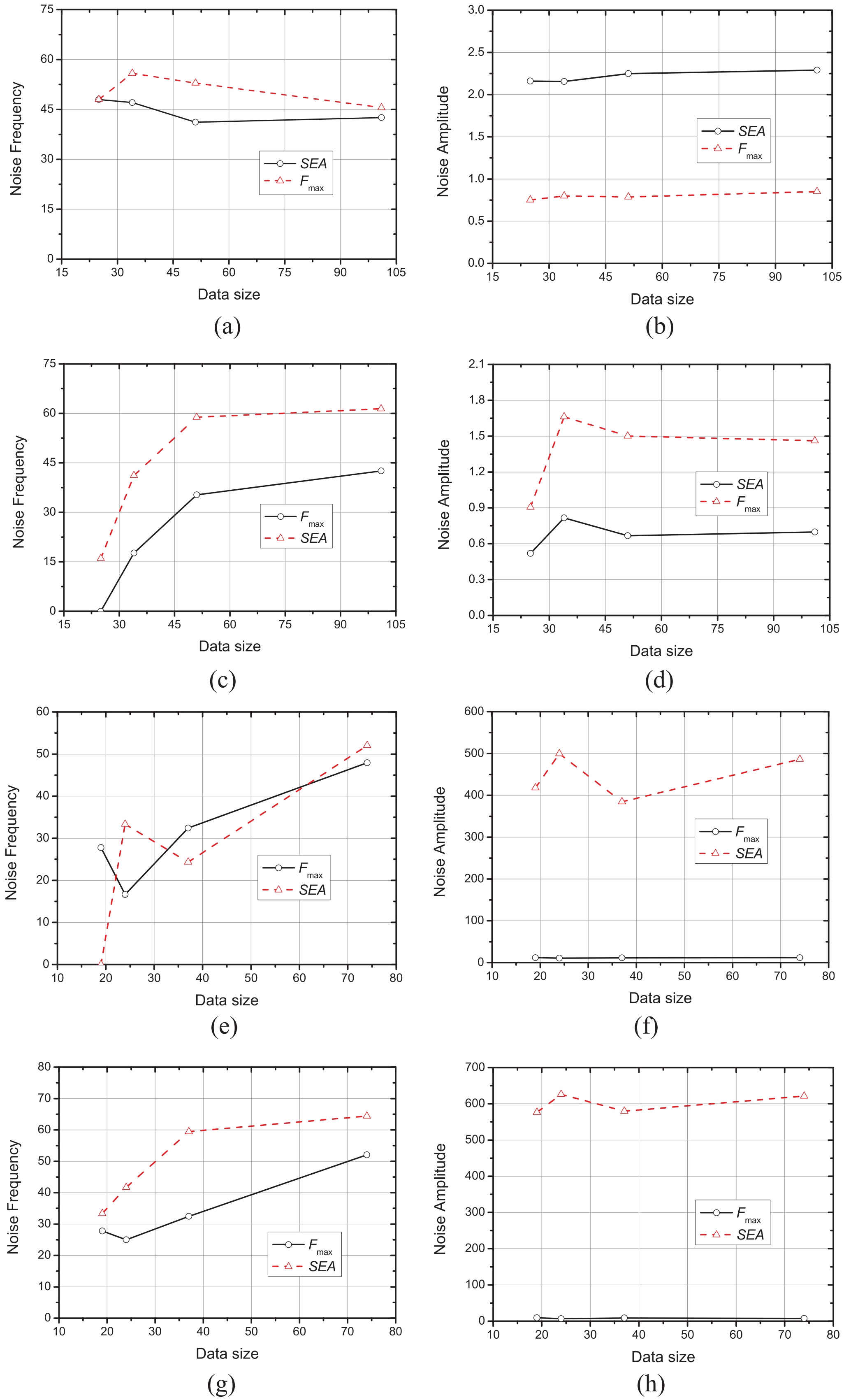

Fig. 9. Noise frequency and amplitude convergence study of data size for different design variable: (a) noise frequency for B in tube example; (b) noise amplitude for B in tube example; (c) noise frequency for t in tube example; (d) noise amplitude for t in tube example; (e) noise frequency for t_1 in front rail example; (f) noise amplitude for t_1 in front rail example; (g) noise frequency for t_2 in front rail example; (h) noise amplitude for t_2 in front rail example.

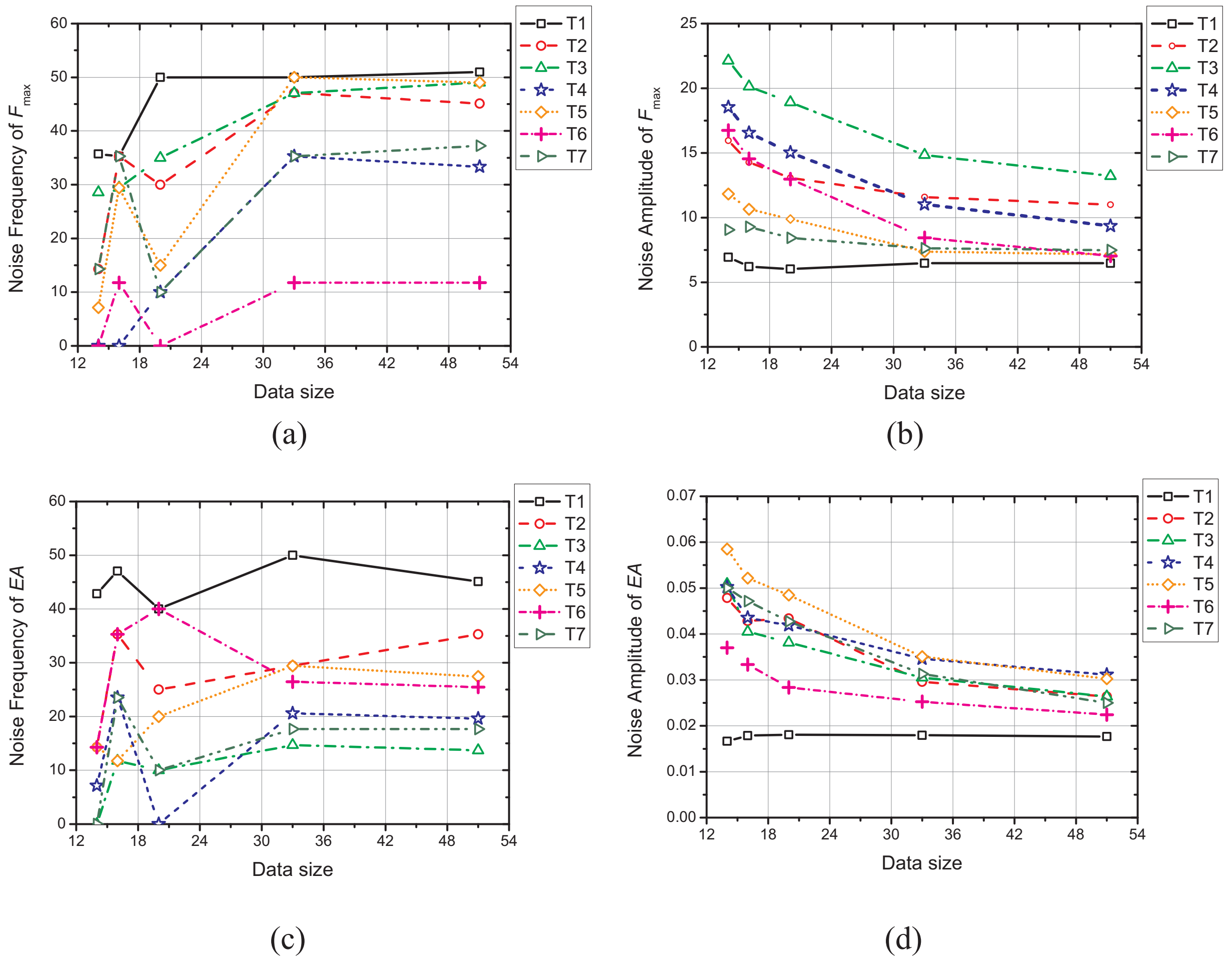

Fig. 10. Noise frequency and amplitude convergence study of data size of 7 design variables for different design criteria: (a) noise frequency for $F_{\max}$ in multi-cell structure example; (b) noise amplitude for $F_{\max}$ in multi-cell structure example; (c) noise frequency for EA in multi-cell structure example; (d) noise amplitude for EA in multi-cell structure example;.

the true response of simulation by taking into account two kinds of uncertainty, as

$$y_{\text{true}}(\mathbf{x}) = y_{\text{surr}}(\mathbf{x}) + e_{\text{surr}} + e_{\text{num}} \tag{14}$$

The rigorous way of handling the two uncertainties is to quantify them by as a statistical distribution. Therefore, e_{surr} and e_{num} are modeled as a statistical distribution. Since the regression process yields $y_{\text{surr}}(\mathbf{x})$ as an unbiased estimate of $y_{\text{true}}(\mathbf{x})$, e_{surr} and e_{num} can be modeled as a normal distribution with a zero mean. Therefore, the estimated $y_{\text{true}}(\mathbf{x})$ has a mean of $y_{\text{surr}}(\mathbf{x})$ and the standard deviation of

$$\sigma = \sqrt{\sigma_{\text{surr}}^2 + \sigma_{\text{num}}^2} \tag{15}$$

In the above equation, it is assumed that e_{surr} and e_{num} are independent, which is not true in reality because the error in the surrogate model is also affected by the error in numerical simulation.

It is well known that e_{surr} can be approximated by the prediction variance of the surrogate model. But, there is no established method to estimate e_{num}, especially when the design changes. From the observation that e_{surr} and e_{num} are not independent, the combined uncertainty is represented using a scalar multiple of the prediction variance. That is

$$\sigma = \sqrt{\sigma_{\text{surr}}^2 + \sigma_{\text{num}}^2} = \lambda\sigma_{\text{surr}} \tag{16}$$

where λ is the level used to quantify both numerical and surrogate uncertainties.

In this paper, we assume that the numerical and surrogate uncertainties are normally distributed, and their uncertainties are proportional to the standard error of the surrogate model. In fact, the polynomial response surface is based on the assumption that the model form is accurate but the data have normally distributed noise. 2-sigma confidence intervals are often used to cover 95% of distribution due to noise in the samples. However, this is true only when the model form of the surrogate is accurate. In reality, the model form is not perfect, as the true model may not be in the form of polynomials. Therefore, if the conventional 2-sigma confidence intervals are utilized to cover 95% of both the model form error and numerical noise, it may not cover the true 95% of simulation results. In fact, numerical noise at the unsampled points also needs to be considered. However, it is hard to separate the model form uncertainty from the numerical uncertainty because the errors in samples include the combined effect. Therefore, instead of separating these two uncertainties, in this paper both uncertainties are assumed to be proportional to the standard error σ_{surr} and estimated by using Eq. (16).

To estimate the level of numerical uncertainty, 101 uniformly distributed points are obtained in the range of each design variable as shown in the convergence study, while the other variable is fixed at $t = 2.5$ or $B = 40$. Fig. 11 shows the variation of $F_{\max}$ and SEA along 101 data for each design variable based on FE model. These FE simulation results are also compared with the second-order PRS fitted with 24 samples. Two findings can be observed from Fig. 11. The first finding is that FE results have a randomly distributed numerical uncertainty as design variables vary. That is, for a small change in design variables, the FE results are scattered in a relatively large amplitude. In addition, if the simulation is repeated at the same design, the results also vary.

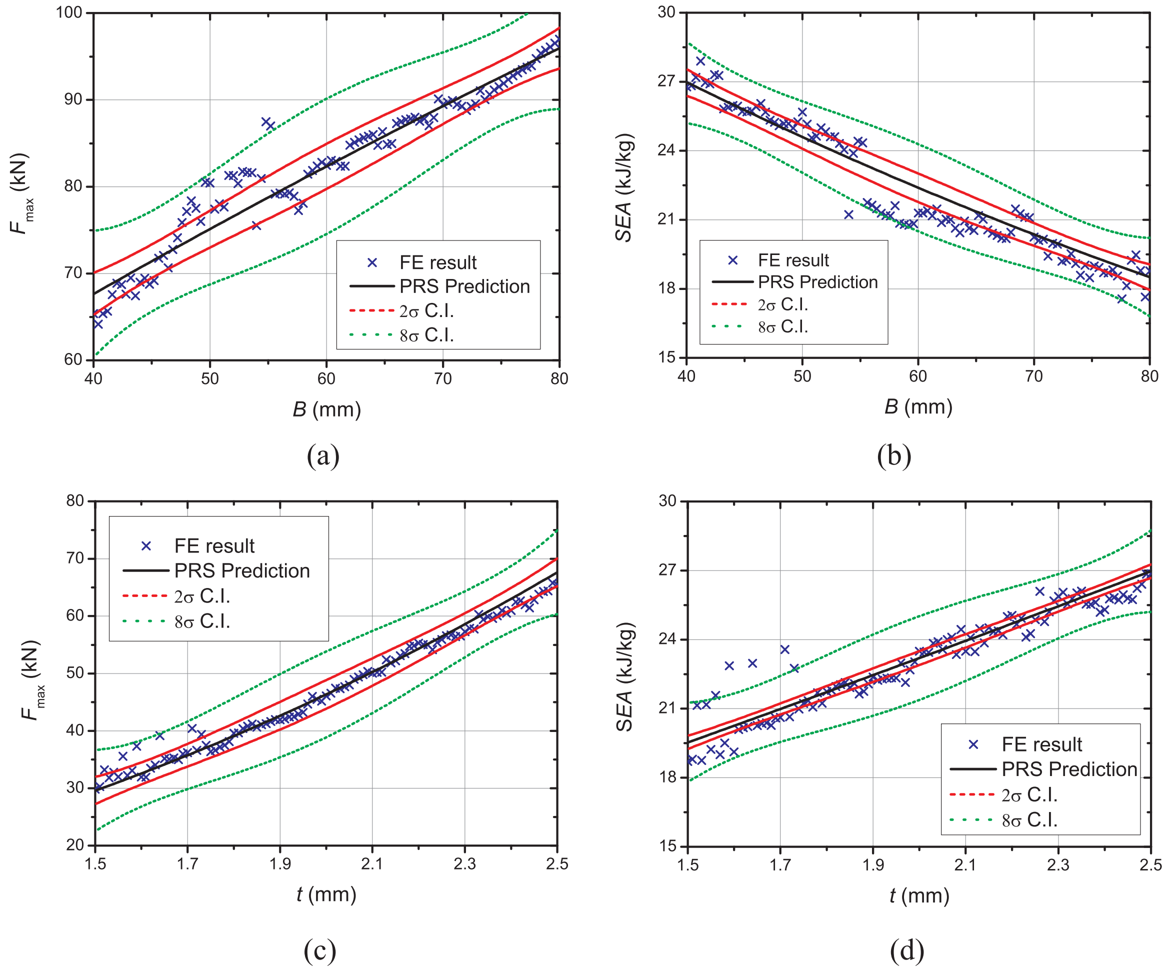

Fig. 11. Comparison of PRS prediction and FEA results for tube example with confidence intervals: (a) F_{max} for different b with t = 2.5 mm; (b) *SEA* for different b with t = 2.5 mm; (c) F_{max} for different t with b = 40 mm; (d) *SEA* for different t with b = 40 mm. (For interpretation of the references to color in this figure, the reader is referred to the web version of this article.)

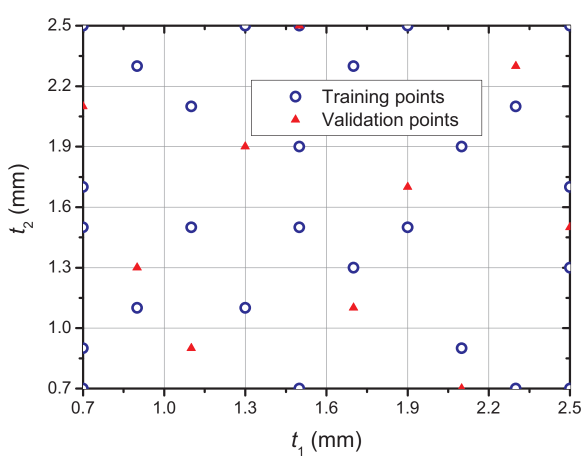

Fig. 12. Training points for the front rail example.

Therefore, the nature of the uncertainty is random as well as biased. This can be confirmed from the trend of errors in Fig. 11(a) and (b). If numerical noise is dominant, then the noise should be randomly distributed with positive and negative errors against the surrogate model predictions (black line in Fig. 11). On the other hand, the model form error may show as a bias.

The other finding is that the conventional 2-sigma confidence intervals, shown in red curves, cannot cover 95% of simulation results, as the actual level of uncertainty is much higher than the 2-sigma confidence intervals shown in Fig. 11(d). This is because the uncertainty is not only from numerical noise but also from surrogate model error. In order to cover 95% of actual simulation results, the confidence intervals should increase to at least 8-sigma, as shown in green curves. Also shown in Fig. 11(a), the errors of the surrogate model and numerical noise depend on the value of design variables. Indeed, the standard error varies with different designs because of surrogate modeling error. Therefore when we use a conservative estimate using λ-sigma, the conservative estimate also varies with designs.

It is noted that it is not the conclusion of this paper that an additional 6-sigma has to be used to compensate for all uncertainties. Rather, the conventional 2-sigma conservative estimate is not sufficient due to the presence of both uncertainties, and different level of conservatism should be used. However, in general, it is difficult to determine the uncertainty factor λ such that λ-sigma confidence intervals can cover 95% of simulation results. In order to have a reliable and robust design, it is necessary to evaluate the uncertainty factor using a similar method presented in Fig. 11.

3.2. Numerical uncertainty and surrogate model uncertainty for front-rail structure

For the front rail example, 20 sample points as shown in Fig. 12 were selected by using Latin hypercube sampling. Besides these, additional 4 corner points (see Fig. 12) of the design space were also used.

Table 2
Accuracy comparison of different orders of PRS surrogate models for front rail example.

		First-order PSR	Second-order PRS	Third-order PRS	Fourth-order PRS
F_{max}	R^2	0.9840	0.9894	0.9945	0.9943
	Adjusted $\bar{R}^2$	0.9825	0.9796	**0.9910**	0.9855
SEA	R^2	0.9680	0.9889	0.9898	0.9886
	Adjusted $\bar{R}^2$	0.9650	0.9591	**0.9833**	0.9709

For PRS surrogate model, the third-order polynomial function was selected based on the same procedure as in the tube example. The adjusted $\bar{R}^2$ of PRS surrogate model was 99.1% and 98.3% for F_{max} and *SEA*, respectively, which indicated that PRS can provide the acceptable accuracy for the following design optimization (Table 2).

According to the tradeoff between the convergence and efficiency as discussed in Section 2.2, data size to quantify numerical noise is determined as 73. It means that one design variable is fixed at 0.7 mm and sampled 73 uniformly distributed points with an interval of 0.25 mm along the other design variable. According to Fig. 13, the 2-sigma intervals (red curves) cannot cover 95% of simulation results, while 4-sigma intervals cover about 98% of simulation results at 73 points. Compared to the confidence intervals of 8-sigma for the tube example, the confidence intervals of 4-sigma for the front rail structure are much smaller. That is because, in the tube example, the number of elements and size will change with the change of width B of the tube, which will cause relatively large numerical noise. However, in the case of the front rail example, the mesh remains constant while the thicknesses of the two plates are changed. Therefore, in this case, 4-sigma is enough to cover 98% of simulation results.

3.3. Numerical uncertainty and surrogate model uncertainty for multi-cell structure

For the multi-cell example, 85 sample points were selected by using Latin hypercube sampling. Extra 10 samples were selected as the validation points. For PRS surrogate model, the third-order polynomial function was selected for F_{max} and second-order for *EA*. The R^2 of PRS surrogate model was 99.4% and 99.7% for F_{max} and *EA*, respectively. Hence the PRS surrogate models were considered accurate and effective for the subsequent design optimization.

As shown in Fig. 14, the PRS predictions with different C.I. for design variable T_1 and T_2 are compared with the FEA results. The comparison figures for other design variables are given in Appendix A. It was observed that the 2-sigma confidence intervals (C.I.) are not enough to cover 95% of simulation results for F_{max} and *EA*, while 4-sigma C.I. can cover about 98% of simulation results for F_{max} and 5-sigma C.I. can generally cover about 95% of simulation results for *EA* at 51 points for every design variable. Therefore, for this example, 4-sigma was utilized for F_{max} and 5-sigma was used for *EA* to cover at least 95% of simulation results.

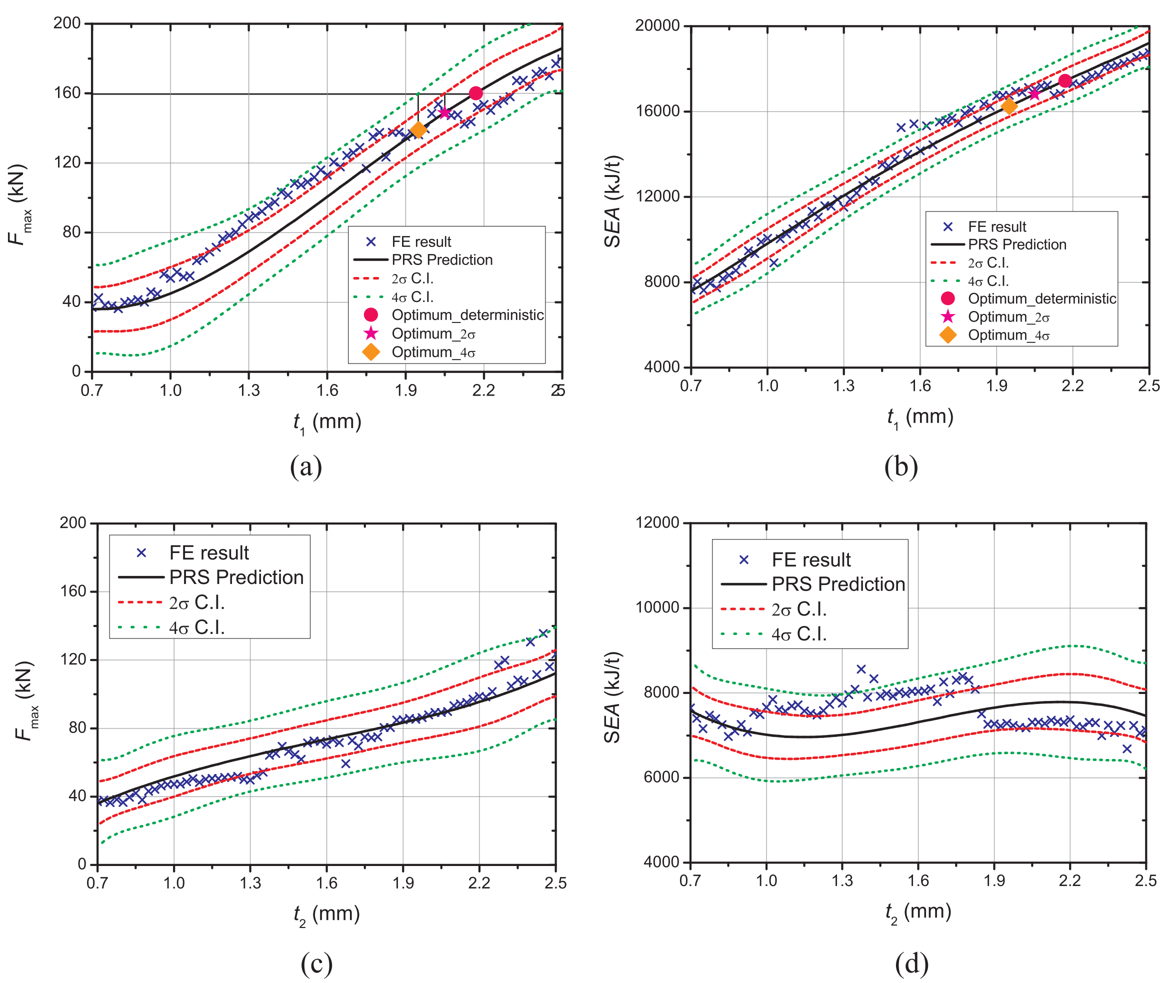

Fig. 13. Comparison of PRS prediction and FEA results for front rail example with confidence intervals: (a) F_{max} for different t_1 with t_2 = 0.7 mm; (b) *SEA* for different t_1 with t_2 = 0.7 mm; (c) F_{max} for different t_2 with t_1 = 0.7 mm; (d) *SEA* for different t_2 with t_1 = 0.7 mm. (For interpretation of the references to color in this figure, the reader is referred to the web version of this article.)

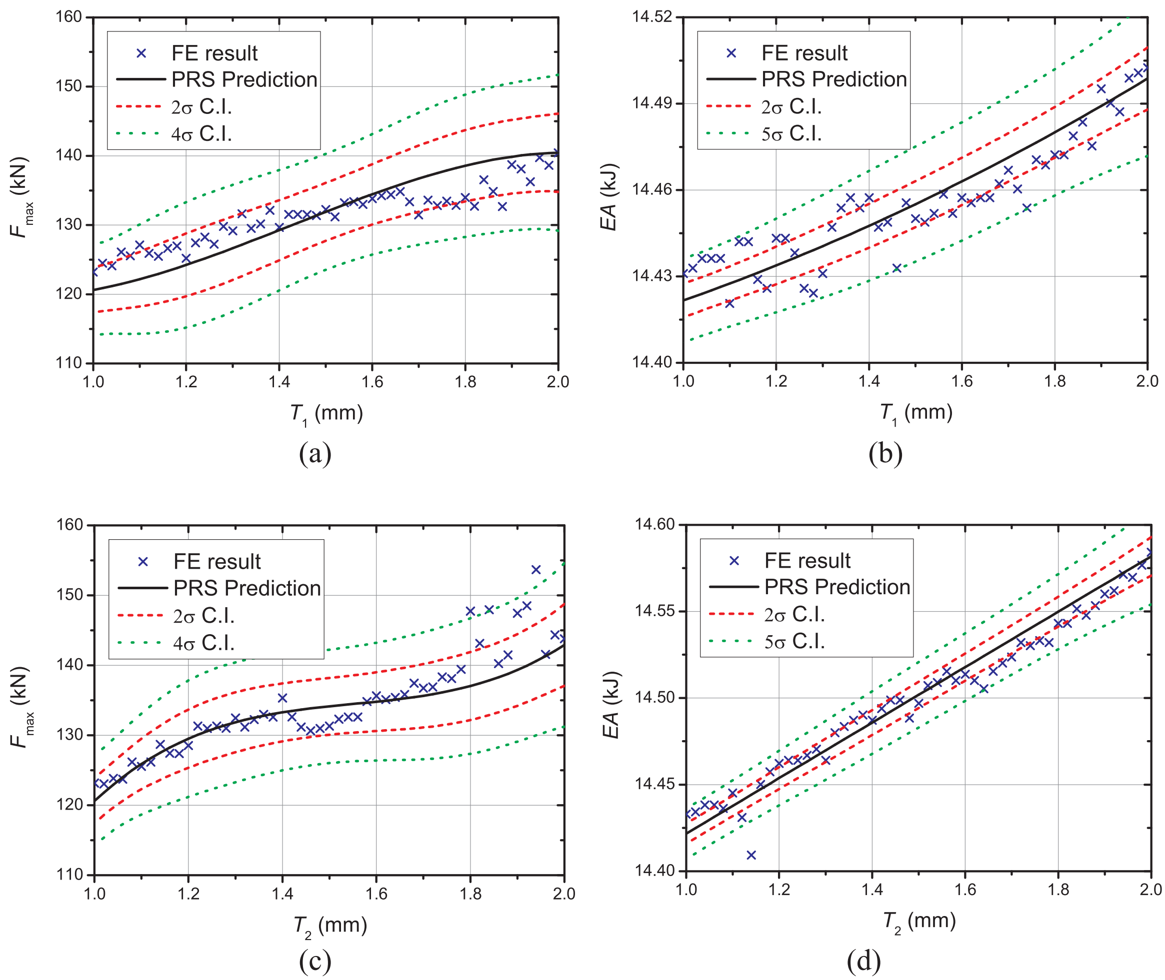

Fig. 14. Comparison of PRS prediction and FEA results for multi-cell structure example with confidence intervals: (a) F_{max} for different T_1; (b) EA for different T_1; (c) F_{max} for different T_2; (d) EA for different T_2.

Table 3
Optimization results of different optimization cases.

		PRS Deterministic	RBRDO 2 σ	RBRDO 8 σ	Optimum from 441 samples
t (mm)		2.44	2.40	2.29	2.35
B (mm)		40.00	40	42.5066	42
F_{max} (kN)	FEA	61.44	60.97	59.52	61.16
	Predict	65.00	63.09	60.10	63.75
	Upper bound of 8 σ C.I.	78.09	75.45	64.95	72.29
SEA (kJ)	FEA	25.95	25.30	26.06	26.54
	Predict	26.54	26.22	24.82	25.53
	Lower bound of 8 σ C.I.	20.71	20.76	20.86	20.96

4. Optimization with uncertainty for crashworthiness

4.1. Optimization with uncertainty for the tube structure

Crash simulation results in Section 2 indicated that the effect of numerical noise is significant and warrants consideration. Thus, to obtain a robust and reliable design, both the numerical uncertainty and surrogate model uncertainty need be considered in the optimization procedure, which is the purpose of this section. An in-house Matlab code of Particle swarm optimization (PSO) algorithm [37] is adopted in this study. The population size for the solver is set as 500 and the generation upper limit is 5000. The solver will stop when either the algorithm reaches the upper limit of generation; i.e., 5000 generations or when there is no improvement for 100 successive generations. The optimization process is repeated five times and yields the same optimum, which shows the statistical convergence of the solutions. The optimization problem is formulated as

$$\begin{cases} \min -\mu(SEA) + \lambda\sigma(SEA) \\ s.\ t. \quad \mu(F_{max}) + \lambda\sigma(F_{max}) \le 65\text{kN} \\ \quad 1.5\text{mm} \le t \le 2.5\text{mm} \\ \quad 40\text{mm} \le B \le 80\text{ mm} \end{cases} \tag{17}$$

where λ is the uncertainty factor to take into account the effect of surrogate model error and numerical noise. $\mu(SEA)$ and $\sigma(SEA)$ are the predictive mean and standard deviation of the objective *SEA* from the PRS. $\mu(F_{max})$ and $\sigma(F_{max})$ are the predictive mean and standard deviation of the constraint F_{max} from the PRS. According to Section 3.1, the λ is set as 2 to consider the 95% confidence interval of the PRS surrogate model error and 8 to cover 95% of the simulation results in terms of both surrogate model error and numerical noise. In addition, since both F_{max} and -*SEA* are the non-beneficial attributes, the positive side is used to make a conservative estimation.

Three different optimization results are presented: (1) deterministic optimization, (2) only considering surrogate-estimated error; i.e., λ = 2, and (3) considering both surrogate model error and numerical

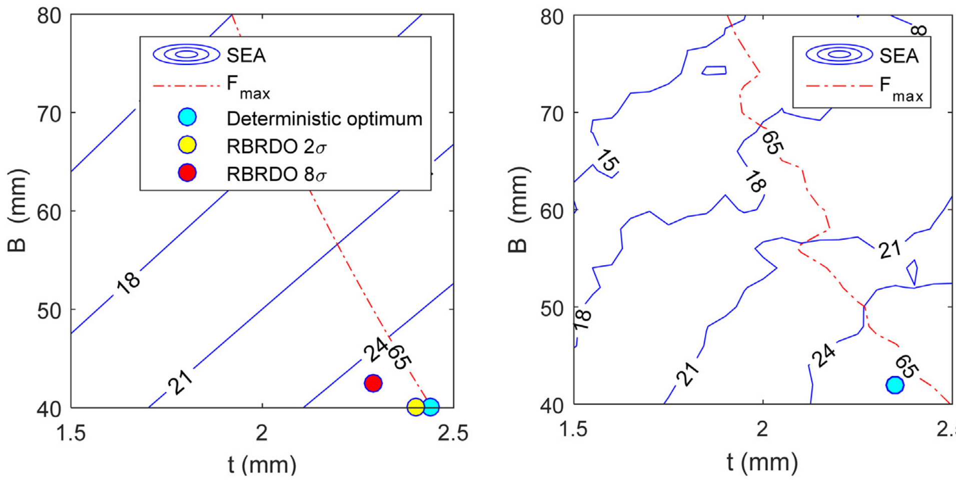

(a) (b)

Fig. 15. Optima and contours of *SEA* and F_{max}: (a) PRS with 24 sampling points; (b) 441 sample points. (For interpretation of the references to color in this figure, the reader is referred to the web version of this article.)

Table 4
Optimization results of different optimization cases for front-rail structure.

		Base-model	PRS Deterministic	RBRDO 2 σ	RBRDO 4 σ
t_1 (mm)		1.889	2.17	2.05	1.95
t_2 (mm)		1.3	0.7	0.7	0.7
F_{max} (kN)	FEA	159.73	151.38	151.44	147.68
	Predict	170.72	160.00	148.81	138.95
	Upper bound of 4 σ C.I.	188.73	181.38	169.85	159.20
SEA (kJ/t)	FEA	15,424.76	17,334.04	17,326.96	17,246.66
	Predict	14,732.49	17,434.78	16,804.78	16,250.35
	Lower bound of 4 σ C.I.	13,883.18	16,554.95	15,879.78	15,311.02

Table 5
Optimization results of different optimization cases for multi-cell tube structure.

		Base-model	PRS Deterministic	RBRDO 2 σ	RBRDO 4/5 σ
T_1 (mm)			2.00	1.18	1.09
T_2 (mm)			1.00	1.78	1.00
T_3 (mm)			1.00	1.00	1.04
T_4 (mm)			2.00	1.08	1.52
T_5 (mm)			1.33	1.20	1.30
T_6 (mm)			1.53	1.33	1.56
T_7 (mm)			1.00	1.00	1.03
F_{max} (kN)	FEA	160	175.74	158.71	152.56
	Predict		160.00	151.81	148.96
	Upper bound of 4 σ C.I.		184.48	168.18	160.00
EA (kJ)	FEA	9.71	14.78	14.70	14.65
	Predict		14.78	14.71	14.66
	Lower bound of 5 σ C.I.		14.74	14.67	14.63

noise; i.e., $\lambda = 8$, and the results are presented in Table 3 and Fig. 15. The PRS-based deterministic optimizations push the design to the constraint boundary of $F_{max} = 65$ kN. Since the optimum design resides on the boundary of the constraint, it is possible that this optimum design can violate the constraint when uncertainty is present.

When only the surrogate model uncertainty is considered, i.e., $\lambda = 2$, the optimum design moves towards the left to the positions indicating a thinner wall (smaller t value) in the feasible region ($F_{max} \leq 65$ kN) shown as a yellow circle in Fig. 15(a). When the numerical uncertainty is also considered, i.e., by changing the value of weight factor λ from 2 to 8, the solution moves further and have a smaller value for t and a larger value for width B. The optimum design moves away from the constraint boundary, thereby guaranteeing a certain level of reliability under uncertainty. In general, the PRS model with $\lambda = 8$ provides an optimum similar to, but more robust and reliable than the optimum design directly selected from 441 sample points (Fig. 15(b)). Therefore, the robustness and performances should be compromised in practice, as shown in the previous research [38]. In addition, for a highly nonlinear crash problem, a large numerical uncertainty and surrogate model uncertainty are present and need be considered to obtain a reliable result.

4.2. Optimization under uncertainty for front rail structure

For the front rail structure example, the optimization problem can be expressed as Eq. (18). Similar to the tube example, three different optimization results are presented. According to the discussion in Section 3.2, the uncertainty factor $\lambda = 4$ is used to take into account both numerical noise and surrogate model error and the results are presented in Table 4.

$$\begin{cases} \min -\mu(SEA) + \lambda\sigma(SEA) \\ s.\ t. \quad \mu(F_{\max}) + \lambda\sigma(F_{\max}) \le 160\text{kN} \\ \quad 0.7\text{mm} \le t_1 \le 2.5\text{mm} \\ \quad 0.7\text{mm} \le t_2 \le 2.5\text{ mm} \end{cases} \tag{18}$$

It is interesting to note that the optimal designs for the three cases were all located at the boundary of design domain $t_2 = 0.7$ mm. This is because *SEA* oscillates within a range but is not improved much as the thickness t_2 increases (see Fig. 13), while $F_{\max}$ increases monotonically. On the other hand, both *SEA* and $F_{\max}$ increase as the thickness t_1 increases. Therefore, a small value of t_2 is preferable to satisfy the constraint on $F_{\max}$. The optimal value of t_2 was obtained to satisfy the upper limit 160 kN with different confidence intervals. As shown in Table 4, the optimal design obtained from deterministic optimization are located at the constraint boundary of $F_{\max} = 160$ kN. However, since the upper bound $F_{\max}$ is 188.73 kN (as shown in Table 4), it can violate the upper limit of the constraint when the surrogate model uncertainty and numerical uncertainty are present. Optimization considering both numerical uncertainty and surrogate model uncertainty can provide a more conservative optimum as shown in Table 4. Notably, the 95% confidence interval (2σ case) of PRS surrogate model is not enough to cover both the numerical uncertainty and surrogate model uncertainty. A more conservative and reliable result can be obtained by considering both uncertainty factors, although the performance will be sacrificed to some degree. However, the final robust and reliable solution can still achieve a 12% increase of *SEA* with a large safety margin.

4.3. Optimization under uncertainty for multi-cell structure

For the multi-cell structure example, the optimization problem can be given as Eq. (19). Three different optimization cases are investigated herein. According to the discussion in Section 3.3, the uncertainty factors for *EA* $\lambda_1 = 5$ and that for $F_{\max}$ $\lambda_2 = 4$ were used to take into account both numerical noise and surrogate model error and the results are presented in Table 5.

$$\begin{cases} \min -\mu(EA) + \lambda_1\sigma(EA) \\ s.\ t. \quad \mu(F_{\max}) + \lambda_2\sigma(F_{\max}) \le 160\text{kN} \\ \quad 1\text{mm} \le T_1, T_2, T_3, T_4, T_5, T_6, T_7 \le 2\text{mm} \end{cases} \tag{19}$$

As shown in Table 5, optimal design obtained from deterministic optimization are located at the constraint boundary of $F_{\max} = 160$ kN. However, $F_{\max}$ obtained from FEA was 174.74, which violates the upper limit of the constraint when the surrogate model uncertainty and numerical uncertainty are present. It indicated that the optimal designs obtained from deterministic design optimization are not reliable. Besides, the 95% confidence interval (2σ case) of PRS surrogate model is not enough to cover both the numerical uncertainty and surrogate model uncertainty. Therefore, 4-sigma and 5-sigma were selected to obtain a more conservative optimum by considering both numerical noise and surrogate models error as shown in Table 5. It is also interesting to note that the final robust and reliable solution for the multi-cell structure can still achieve a 50% increase of *EA* than the baseline model of front-rail absorbers. It shows that multi-cell structure is very promising in improving the crashworthiness performance as energy absorbers.

5. Conclusions

Numerical noise is an inevitable by-product for the crashworthiness simulations for their highly nonlinear responses. This issue can lead to challenges in finding robust and reliable optimum designs. To solve this issue, the paper presented a novel method to determine the number of data for estimating the accurate level of numerical noise. More importantly, a simple quantification method to consider numerical uncertainty and surrogate model uncertainty was proposed in optimization under uncertainty based on the standard error of PRS surrogate model. It was observed that the conventional 95% confidence interval is not enough for robustness especially when the level of noise in the simulation is high because the number of samples to build a surrogate is normally too small for accurately estimating the level of noise. It was shown that the different confidence intervals should be chosen based on the level of noise. For the numerical examples considered, it was demonstrated that about 8-sigma is required when the mesh is changed at different designs, while 4-sigma is enough when the mesh does not change.

Acknowledgment

This work was supported by The National Natural Science Foundation of China (51575399) and The National Science & Technology Program during the Thirteenth Five-Year Plan Period (2016YFB0101600). The first author is a recipient of the doctoral scholarships from China Scholarship Council (CSC).

Appendix A

See Appendix Fig. A1.

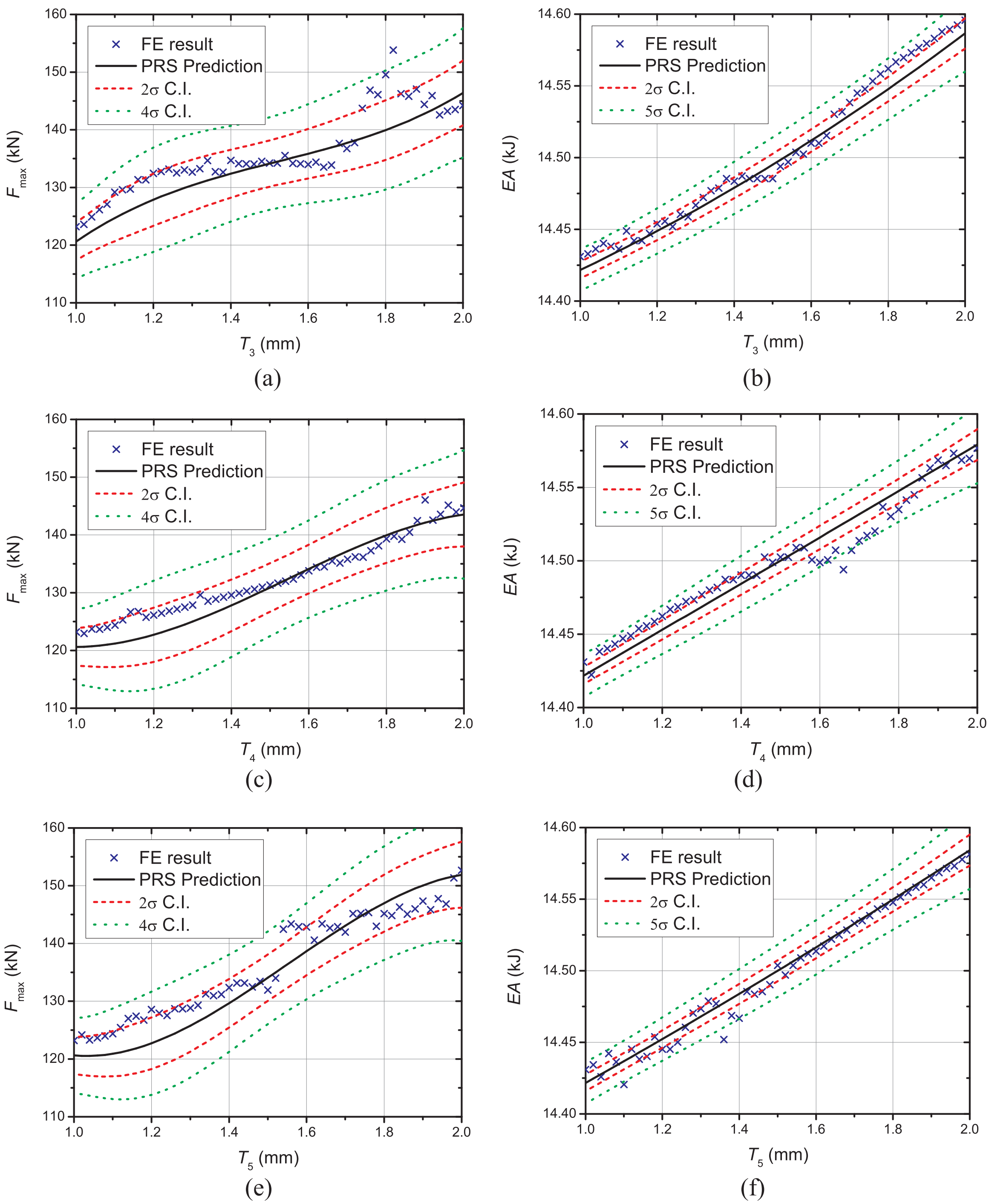

Fig. A1. Comparison of PRS prediction and FEA results for multi-cell structure example with confidence intervals: (a) F_{max} for different T_3; (b) EA for different T_3; (c) F_{max} for different T_4; (d) EA for different T_4; (e) F_{max} for different T_5; (f) EA for different T_5; (g) F_{max} for different T_6; (h) EA for different T_6; (m) F_{max} for different T_7; (n) EA for different T_7.

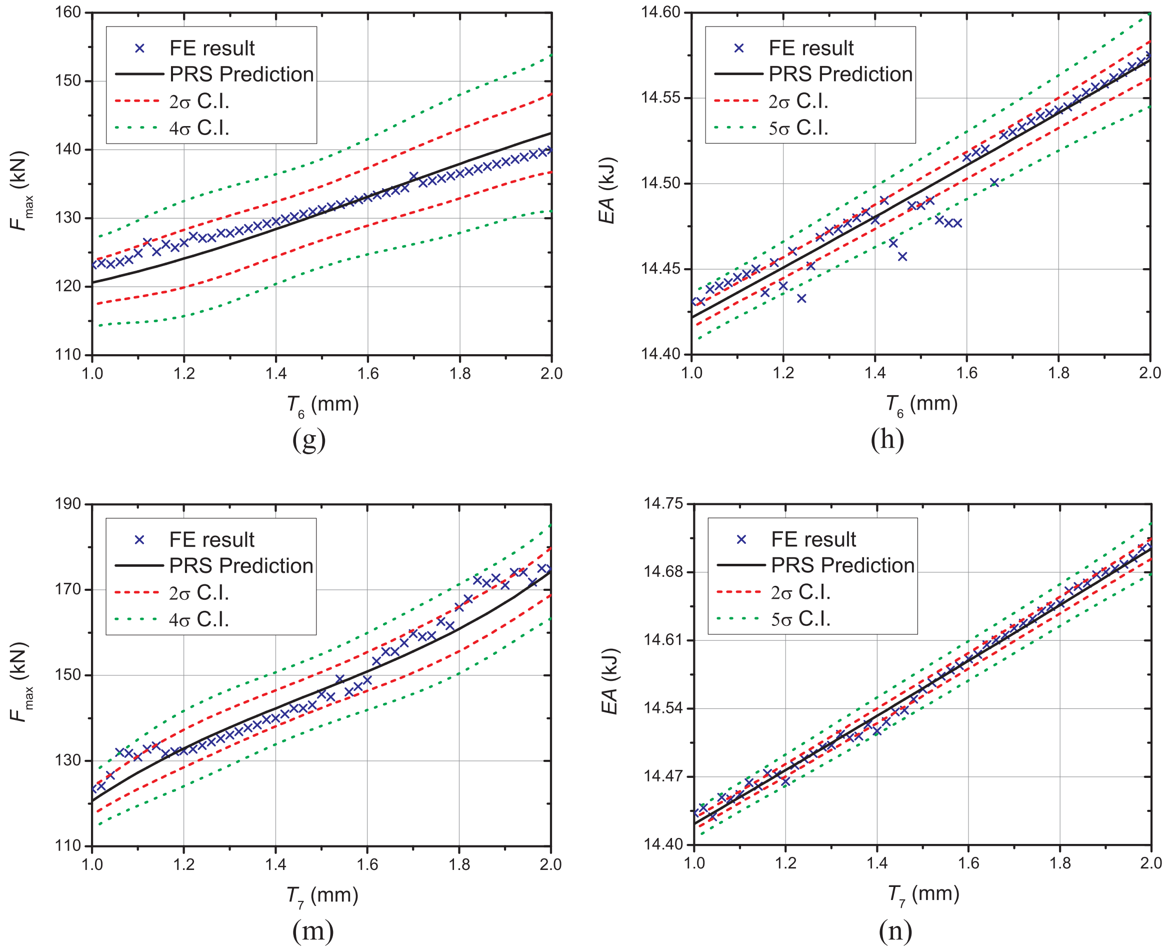

Fig. A1. (*continued*)

References

[1] C.A. Gilkeson, V.V. Toropov, H.M. Thompson, M.C.T. Wilson, N.A. Foxley, P.H. Gaskell, Dealing with numerical noise in CFD-based design optimization, Comput. Fluids 94 (2014) 84–97.

[2] G.J. Park, S. Xu, S. Yoon, S.B. Jeong, Non-linear dynamic response structural optimization of an automobile frontal structure using equivalent static loads, Proc. Inst. Mech. Eng. Part D: J. Automob. Eng. 224 (4) (2010) 489–501.

[3] F. Duddeck, Multidisciplinary optimization of car bodies, Struct. Multidiscip. Optim. 35 (4) (2007) 375–389.

[4] J. Will, State of the art–robustness evaluation in CAE-based virtual prototyping processes of automotive applications, Proc. Optim. Stoch. Days 4 (2007).

[5] F. Duddeck, H. Zimmer, New achievements on implicit parameterization techniques for combined shape and topology optimization for crashworthiness based on SFE concept, Shape Technol. Optim. Crashworthiness, ICRASH2012 (2012).

[6] C.-.A. Thole, L. Mei, Reasons for scatter in crash simulation results, in: Proceedings of the 4th European LS-DYNA Users' Conference, Ulm, Germany, 2003.

[7] J. Will, H. Baldauf, C. Bucher, Robustness evaluations in virtual dimensioning of passive passenger safety and crashworthiness, in: Proceedings Weimarer Optimierungs-und Stochastiktage 3, 2006.

[8] J. Fang, Y. Gao, G. Sun, C. Xu, Q. Li, Multiobjective robust design optimization of fatigue life for a truck cab, Reliab. Eng. Syst. Saf. 135 (2015) 1–8.

[9] G.-J. Park, T.-H. Lee, K.H. Lee, K.-H. Hwang, Robust design: an overview, AIAA J. 44 (1) (2006) 181–191.

[10] H.-G. Beyer, B. Sendhoff, Robust optimization – a comprehensive survey, Comput. Methods Appl. Mech. Eng. 196 (33–34) (2007) 3190–3218.

[11] W. Yao, X. Chen, W. Luo, M. van Tooren, J. Guo, Review of uncertainty-based multidisciplinary design optimization methods for aerospace vehicles, Prog. Aerosp. Sci. 47 (6) (2011) 450–479.

[12] J. Fang, Y. Gao, G. Sun, Q. Li, Multiobjective reliability-based optimization for design of a vehicledoor, Finite Elem. Anal. Des. 67 (2013) 13–21.

[13] J. Fang, Y. Gao, G. Sun, Y. Zhang, Q. Li, Crashworthiness design of foam-filled bitubal structures with uncertainty, Int. J. Non-Linear Mech. 67 (2014) 120–132.

[14] S. Ghanmi, M.L. Bouazizi, N. Bouhaddi, Robustness of mechanical systems against uncertainties, Finite Elem. Anal. Des. 43 (9) (2007) 715–731.

[15] S.-i. Sakata, I. Torigoe, A successive perturbation-based multiscale stochastic analysis method for composite materials, Finite Elem. Anal. Des. 102–103 (2015) 74–84.

[16] S. Shang, G.J. Yun, Stochastic finite element with material uncertainties: implementation in a general purpose simulation program, Finite Elem. Anal. Des. 64 (2013) 65–78.

[17] S. Zhang, P. Zhu, W. Chen, Crashworthiness-based lightweight design problem via new robust design method considering two sources of uncertainties, Proc.e Inst. Mech. Eng. Part C: J. Mech. Eng. Sci. 227 (7) (2012) 1381–1391.

[18] S. Zhang, P. Zhu, W. Chen, P. Arendt, Concurrent treatment of parametric uncertainty and metamodeling uncertainty in robust design, Struct. Multidiscip. Optim. 47 (1) (2012) 63–76.

[19] V. Picheny, N.H. Kim, R.T. Haftka, Application of bootstrap method in conservative estimation of reliability with limited samples, Struct. Multidiscip. Optim. 41 (2) (2009) 205–217.

[20] F.A.C. Viana, V. Pecheny, R.T. Haftka, Using cross validation to design conservative surrogates, AIAA J. 48 (10) (2010) 2286–2298.

[21] C. Kim, K.K. Choi, Reliability-based design optimization using response surface method with prediction interval estimation, J. Mech. Des. 130 (12) (2008) 121401.

[22] R. Blumhardt, Numerische Optimierung des Crashverhaltens von Fahrzeugstrukturen und-komponenten, Shaker, 2002.

[23] N. Qiu, Y. Gao, J. Fang, Z. Feng, G. Sun, Q. Li, Theoretical prediction and optimization of multi-cell hexagonal tubes under axial crashing, Thin-Walled Struct. 102 (2016) 111–121.

[24] N. Qiu, Y. Gao, J. Fang, Z. Feng, G. Sun, Q. Li, Crashworthiness analysis and design of multi-cell hexagonal columns under multiple loading cases, Finite Elem. Anal. Des. 104 (2015) 89–101.

[25] J. Fang, Y. Gao, G. Sun, G. Zheng, Q. Li, Dynamic crashing behavior of new extrudable multi-cell tubes with a functionally graded thickness, Int. J. Mech. Sci. 103 (2015) 63–73.

[26] J. Fang, Y. Gao, G. Sun, N. Qiu, Q. Li, On design of multi-cell tubes under axial and oblique impact loads, Thin-Walled Struct. 95 (2015) 115–126.

[27] X. Song, G. Sun, G. Li, W. Gao, Q. Li, Crashworthiness optimization of foam-filled tapered thin-walled structure using multiple surrogate models, Struct. Multidiscip. Optim. 47 (2) (2012) 221–231.

[28] G. Sun, T. Pang, J. Fang, G. Li, Q. Li, Parameterization of criss-cross configurations for multiobjective crashworthiness optimization, Int. J. Mech. Sci. 124–125 (2017) 145–157.

[29] J. Fang, G. Sun, N. Qiu, G.P. Steven, Q. Li, Topology optimization of multicell tubes under out-of-plane crushing using a modified artificial bee colony algorithm, J. Mech. Des. 139 (7) (2017) 071403.
[30] T. Belytschko, J.I. Lin, T. Chen-Shyh, Explicit algorithms for the nonlinear dynamics of shells, Comput. Methods Appl. Mech. Eng. 42 (2) (1984) 225–251.
[31] X. Zhang, H. Zhang, Energy absorption of multi-cell stub columns under axial compression, Thin-Walled Struct. 68 (2013) 156–163.
[32] Y. Zhang, G. Sun, G. Li, Z. Luo, Q. Li, Optimization of foam-filled bitubal structures for crashworthiness criteria, Mater. Des. 38 (2012) 99–109.
[33] N. Qiu, Y. Gao, J. Fang, G. Sun, N.H. Kim, Topological design of multi-cell hexagonal tubes under axial and lateral loading cases using a modified particle swarm algorithm, Appl. Math. Model. 53 (2018) 567–583, http://dx.doi.org/10.1016/j.apm.2017.08.017.
[34] M. Papila, R.T. Haftka, Response surface approximations: noise, error repair, and modeling errors, AIAA J. 38 (12) (2000) 2336–2343.
[35] M.D. McKay, R.J. Beckman, W.J. Conover, Comparison of three methods for selecting values of input variables in the analysis of output from a computer code, Technometrics 21 (2) (1979) 239–245.
[36] A.I. Khuri, S. Mukhopadhyay, Response surface methodology, Wiley Interdiscip. Rev.: Comput. Stat. 2 (2) (2010) 128–149.
[37] C.A.C. Coello, G.T. Pulido, M.S. Lechuga, Handling multiple objectives with particle swarm optimization, IEEE Trans. Evolut. Comput. 8 (3) (2004) 256–279.
[38] G.I. Schuëller, H.A. Jensen, Computational methods in optimization considering uncertainties–an overview, Comput. Methods Appl. Mech. Eng. 198 (1) (2008) 2–13.